Nuclear Science and Techniques (2025) 36:89
https://doi.org/10.1007/s41365-025-01660-0

Performance study of THGEM-based semicylindrical TPC for intermediate-energy charge-exchange reaction experiments in inverse kinematics

Zhi-Xuan He[1,2] · Pan-Jiao Shen[1,2] · Jing-Yan Wang[1,2] · Wen-Juan Bu[1,2] · Zhou-Bo He[3,4] · Zhi-Jie Li[3,4] · Yuan-Sheng Yang[3,4] · Xiao-Lei Chen[1,2] · Chen-Gui Lu[3,4] · Peng Ma[3,4] · He-Run Yang[3,4] · Li-Min Duan[3,4] · Bi-Tao Hu[3,4] · Xiang-Lun Wei[3,4] · Yi Zhang[1,2]

Received: 3 September 2024 / Revised: 26 November 2024 / Accepted: 6 December 2024 / Published online: 20 March 2025

Abstract

The semicylindrical time projection chamber (scTPC) is designed to measure the angular distribution of the cross section for intermediate-energy (^{3}He,t) charge-exchange reactions in inverse kinematics. The scTPC prototype comprises a cathode, field cage, drift region, amplification structure based on a multilayer thick gas electron multiplier (THGEM), and a readout plane with 886 zigzag-shaped pads. The gain uniformity of the THGEM and the drift velocity of electrons were calibrated. Track recognition based on the Hough transform was then developed to reconstruct cosmic ray tracks and determine their position resolution. The position resolution of secondary particle tracks resulting from collisions between the heavy-ion beam and the ^{3}He target was measured, yielding an x-resolution of 0.71 mm and a z-resolution of 0.73 mm. The scTPC demonstrates sufficient energy and spatial resolution to support charge-exchange reaction experiments in inverse kinematics.

Keywords Charge-exchange reaction · Time projection chamber · Track recognition · Track reconstruction

1 Introduction

The charge-exchange reaction, a type of direct nuclear reaction, serves as a valuable experimental tool for exploring the intricate structure of atomic nuclei, particularly through the lens of spin-isospin excitation [1, 2]. Reactions such as (^{3}He,t), (t,^{3}He), and (d,^{2}He) are widely employed in charge-exchange studies due to their high resolution and detection efficiency [3–7]. On the theoretical side, the distorted wave born approximation (DWBA) is a commonly used theoretical framework for analyzing reaction cross sections. Furthermore, a research group at Peking University developed an improved Eikonal method, achieving better agreement with experimental data across a wide energy range [8, 9]. Experimentally, charge-exchange reactions such as (^{3}He,t) and (t,^{3}He) have been studied for various nuclei using ^{3}He and triton beams produced by accelerators. For instance, researchers at the Institute of Modern Physics measured the Gamow–Teller strength distribution of the odd-mass nucleus ^{93}Nb using a triton beam at 115 MeV/u from the coupled cyclotron facility (CCF) at the National Superconducting Cyclotron Laboratory (NSCL) [10]. Exclusive measurements

This work was supported by National Key R&D Program of China (No. 2022YFE0103900), the National Natural Science Foundation of China (Nos. 11875301, 11875302, U1867214, U1832105, U2032166 and U1832167), the Fundamental Research Funds for the Central Universities (No. lzujbky-2022-sp06), the CAS "Light of West China" Program, and the Heavy Ion Research Facility in Lanzhou.

✉ Xiang-Lun Wei
weixl@impcas.ac.cn

✉ Yi Zhang
yizhang@lzu.edu.cn

[1] School of Nuclear Science and Technology, Lanzhou University, Lanzhou 730000, China

[2] Frontiers Science Center for Rare Isotopes, Lanzhou University, Lanzhou 730000, China

[3] Institute of Modern Physics, Chinese Academy of Science, Lanzhou 730000, China

[4] School of Nuclear Science and Technology, University of Chinese Academy of Sciences, Beijing 101408, China

of the ^{59}Co(t,^{3}He+γ)^{59}Fe reaction enabled the first determination of Gamow–Teller strengths from low-lying states in ^{59}Fe to its ground state ^{59}Co [11]. These experimental efforts have yielded significant insights in nuclear astrophysics, particularly in understanding the late stages of core-collapse supernovae. Additionally, charge-exchange reactions are pivotal in the study of nuclear structures, including isospin excitations, giant resonances, β-decay, and the neutron skin thickness of nuclei. However, experimental studies of the charge-exchange reaction have largely been limited to stable nuclides due to current experimental constraints. Hence, conducting charge-exchange reaction experiments on unstable nuclides in inverse kinematics remains challenging but is a promising research frontier. For the first time, a research team at Michigan State University successfully extracted the Gamow–Teller transition strength, B(GT), in the β^+ direction from an unstable nucleus using the (d,^{2}He) reaction in inverse kinematics. This milestone was achieved through the combined use of an active-target time projection chamber (AT-TPC) and a magnetic spectrometer, providing a robust solution for conducting inverse kinematics experiments [12, 13].

The Heavy Ion Research Facility in Lanzhou (HIRFL) is a prominent nuclear physics experimental facility in China, hosting numerous groundbreaking experiments. A research group from Beihang University measured charge-changing cross sections of exotic nuclei at the Radioactive Ion Beam Line in Lanzhou (RIBLL) to extract charge radii and investigate the structure of exotic nuclei [14, 15]. Researchers from the Institute of Modern Physics successfully measured cross sections for single-neutron removal, two-neutron removal, and one-proton knockout reactions on a carbon target at a beam energy of approximately 240 MeV/u at the External Target Facility (ETF) [16–18]. Additionally, the breakup reaction of ^{9}Li on a Pb target at 32.7 MeV/u was measured for the first time at RIBLL by researchers from the Institute of Modern Physics and Lanzhou University [19].Given these achievements, the HIRFL is expected to play a crucial role in advancing charge-exchange reaction research [20]. One such application involves (^{3}He,t) charge-exchange reaction experiments in inverse kinematics, where a ^{3}He target is bombarded with a radioactive beam generated by the HIRFL to study unstable neutron-rich nuclides. To explore the feasibility of (^{3}He,t) experiments in inverse kinematics using a heavy-ion beam, we designed and constructed a detection system for large-angle scattering tritons (t). The detection system is based on a ΔE-E telescope configuration, where the ΔE detector is a semicylindrical time projection chamber (scTPC), and the E detector is a CsI(Tl) array [21]. The CsI(Tl) array offers excellent energy detection capabilities, facilitating efficient particle identification [22].

The time projection chamber (TPC) is a versatile detector capable of accurately measuring the scattering angle θ of secondary particles by reconstructing three-dimensional tracks and providing precise energy measurements [23]. Consequently, TPCs have been extensively utilized in nuclear physics experiments [24–31]. For instance, researchers at Peking University developed a compact active-target time projection chamber (CAT-TPC) to investigate resonant scattering related to cluster structures in unstable nuclei, achieving an angular resolution of approximately 0.45 degree [27, 28]. To meet the demands of the cooling storage ring external-target experiment (CEE), a TPC prototype was designed and tested using pulsed ultraviolet laser beams. Testing demonstrated excellent performance in both track and energy resolution [29]. In addition, the High-energy Fragment Separator (HFRS), currently under construction, incorporates multiple sets of position-sensitive twin TPC detectors for particle identification and beam monitoring [30]. Similarly, a multipurpose time projection chamber (MTPC) has been developed to measure cross sections of neutron-induced nuclear reactions at the back-streaming white neutron facility (Back-n) of the China Spallation Neutron Source [31].

The semicylindrical detector design was chosen to reserve space for future heavy-ion nuclear reaction experiments utilizing a polarized ^{3}He target. The nuclei in ^{3}He gas can be polarized (aligned in the same spin direction) through a spin-exchange optical pumping (SEOP) process [32]. In this setup, the polarized ^{3}He target is bombarded by an intermediate- or high-energy heavy-ion beam, enabling the selection of specific coupling terms and providing insight into the spin-related components of nuclear interactions [33]. Experiments in inverse kinematics further extend the range of atomic nuclei that can be studied. The polarized ^{3}He target is based on a design similar to the ^{3}He glass cell developed at Lanzhou University [34], featuring a spherical glass chamber above the target tube, constructed from aluminosilicate (GE180) glass, as shown in Fig. 1. During the polarization process, ^{3}He gas is polarized in the spherical chamber and then transported through a transmission pipe into the cylindrical target chamber. To maintain polarizability, a magnetic field of approximately 50 G is applied to the ^{3}He target using Helmholtz coils. This field also extends to the TPC, but the low field strength ensures a negligible effect on charged particle tracking. Hence, a semicylindrical structure considering these factors must be implemented. However, we initially plan to perform experiments with a non-polarized ^{3}He target. Hence, the employed target is a non-polarized, as described in Sect. 3.6.

This study focused on evaluating the performance of the scTPC component of the detector. The assessment was conducted using a combination of radioactive sources, UV lasers, cosmic ray muons, and heavy-ion beams. First, the energy resolution and gain inhomogeneity of the THGEM were tested using a ^{55}Fe X-ray source, which provided a

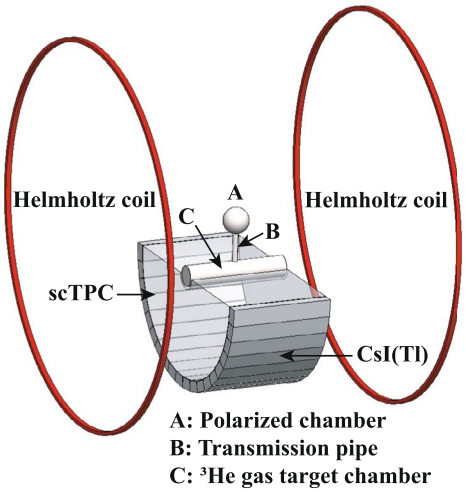

Fig. 1 Schematic of the polarized ^{3}He target device

normalized gain correction factor for each channel. Subsequently, the drift velocity of electrons in the scTPC was calibrated using both laser signals and cosmic rays, with the results from these two methods showing good agreement. Track reconstruction for cosmic ray and beam tests was performed using a recognition algorithm based on the Hough transform. The position resolution of cosmic ray tracks was also measured. In later tests, the heavy-ion beam was directed at the ^{3}He target, and the secondary charged particles produced in the collision were detected using the scTPC. Their tracks were reconstructed to determine both position and angular resolutions. The structure of the detector is outlined in Sect. 2, while the performance test results are presented in Sect. 3. A summary of the findings is provided in Sect. 4.

2 Experimental setup

The TPC section of the detector (refer to Refs. [21] for a comprehensive description of the detector construction), as shown in Fig. 2, consists of a cathode board, a field cage, two layers of THGEM films, and a readout electrode. The detailed scTPC parameters are listed in Table 1. The cathode is a single-sided copper-coated PCB (printed circuit board). The field cage is a semicylindrical structure, with an inner radius of 25 mm and an outer radius of 197 mm, made from a flexible PCB. Uniformly distributed copper-coated electrode strips are present on both sides of the PCB. Each electrode strip has a width of 1.5 mm, with a 2 mm pitch between the centers of adjacent strips. The voltage gradient in the field cage is supplied by a voltage divider circuit consisting of 198 1 MΩ series resistors. The amplification structure consists of a double-layer THGEM [35, 36], with high voltage supplied by a voltage-divider circuit, as shown in Fig. 3. To limit the total charge during discharge [37], one side of the THGEM is partitioned into six fan-shaped segments, with a 1 mm gap between adjacent segments, as illustrated in Fig. 4. Each segment is connected to a common high-voltage distribution via a 10 MΩ resistor, ensuring that the potential of each segment remains consistent. THGEM 1 has a partitioned side on the lower surface, while THGEM 2 has a partitioned side on the upper surface. The readout electrode consists of 886 zigzag-shaped pads [38], each measuring 7.29 mm in the vertical direction and 3.43 mm in the horizontal direction. The readout electronics and data acquisition systems for the scTPC are based on ASICs for General Electronics for TPC (AGET) chips [39, 40]. A gas mixture of Ar-iC_4 H_{10} is commonly used in THGEM tests [41, 42] due to its high gain and fast drift velocity. For the THGEM-based scTPC, a gas mixture of Ar-iC_4 H_{10} (95:5) [42] was selected as the operating gas.

3 Performance test

3.1 Waveform fit

The AGET output waveform has an asymmetric shape, as shown in Fig. 5. A fitting function is used to fit the waveform to extract information from the signal waveform, mainly temporal (e.g., peak position) and amplitude information. The waveform is fitted using the following function [31]:

$$f(t) = B + A\left(\frac{t-t_0}{\tau}\right)^3 \exp\left(\frac{t-t_0}{\tau}\right)\Theta(t-t_0), \tag{1}$$

where B represents the baseline of the waveform, A is a quantity related to the amplitude of the waveform, t_0 is the starting time, τ is the electronics shaping time, and Θ is the Heaviside step function, which has the functional form:

$$\Theta(t-t_0) = \begin{cases} 0, & t-t_0 < 0 \\ \frac{1}{2}, & t-t_0 = 0 \\ 1, & t-t_0 > 0 \end{cases}. \tag{2}$$

To calculate the amplitude, we first determine the maximum value of the fitting function within the region where the waveform is located and subtract the baseline. The resulting value is referred to as the Amplitude. The position at which the Amplitude occurs is the peak position (peakPos). Additionally, the time information of the charged particle is extracted using constant fraction discrimination (CFD), specifically at 20% of the Amplitude, which is denoted as CFDRisingTime. The initial values of the fitting function parameters vary depending on the sampling frequency

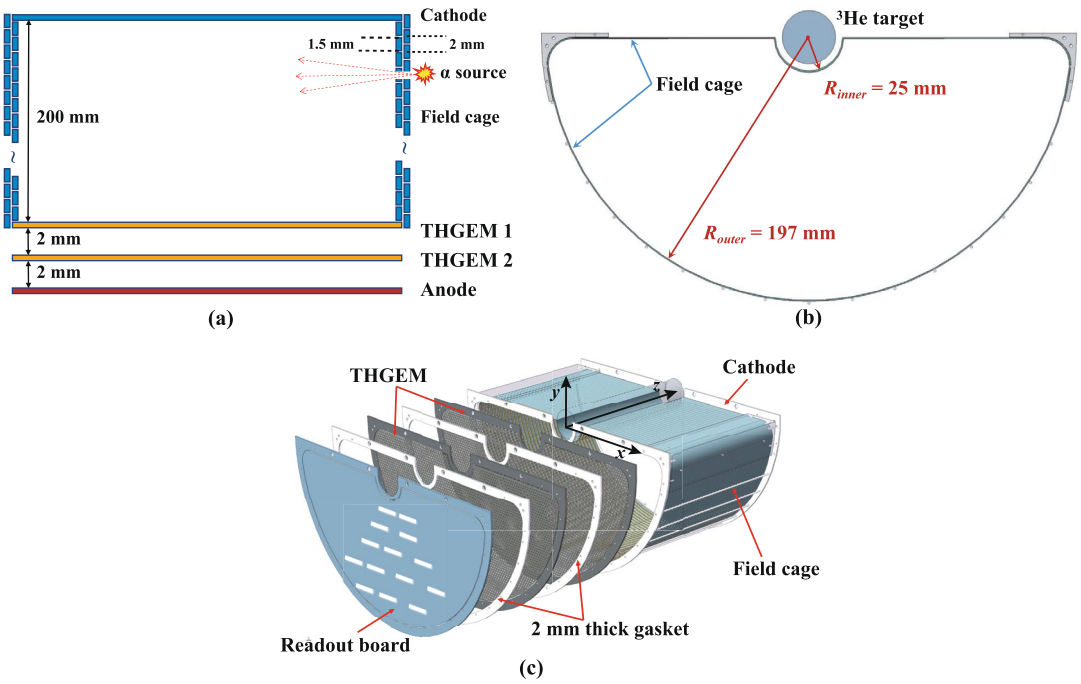

Fig. 2 (Color online) Schematic view of the scTPC structure. The drift region, extending from the cathode to the upper surface of THGEM 1, has a length of 200 mm. The transfer gap between the two THGEM foils is 2 mm, and the depth of the induction region is also 2 mm

Table 1 Parameters of scTPC

Items	Parameters
Operating gas	Ar (95%) + iC_4H_{10} (5%)
Gas pressure (mbar)	850
Maximum drift length (mm)	200
Length of transfer region (mm)	2
Length of induced region (mm)	2
Inner radius of field cage (mm)	25
Outer radius of field cage (mm)	197
Width of field cage electrode strip (mm)	1.5
Pitch of field cage electrode strips (mm)	2
Height of Zigzag-shaped pad (mm)	7.29
Width of Zigzag-shaped pad (mm)	3.43
Total number of effective pads	886
Drift electric field (V/(cm atm))	200
THGEM 1 voltage (V)	650
THGEM 2 voltage (V)	600

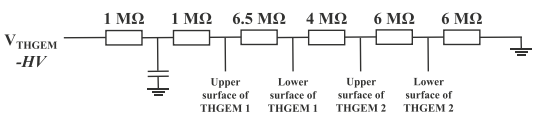

Fig. 3 Voltage divider circuit of multilayer THGEM

and shaping time of the AGET. The signals of X-rays and charged particles (such as α particles) were fitted as shown in Fig. 5. For X-rays, which are point sources, the raw pulse signal induced on the readout pad can be approximated as a δ-like function. In contrast, for charged particles such as α particles, the raw pulse has a certain width because the signal collected by the pad corresponds to a short section of the track. The adopted fitting function effectively describes the waveforms of both types of signals.

3.2 X-ray test

The field cage was temporarily removed for the ^{55}Fe source test. The voltage divider circuit for the THGEM power supply remained consistent with those used in other tests, as shown in Fig. 3. The cathode consisted of a 25 μm thick double aluminized Mylar film, and the ^{55}Fe source was placed outside the drift region, directly in front of the cathode film. The length of the drift region was 4 mm.

X-rays deposit their entire energy at a single point in the operating gas, resulting in a small electron cloud produced by single X-ray photon ionization. This typically generates a signal on one or two pads. Different positions on the THGEM were irradiated using the X-ray source. By selecting events in which only one pad was triggered, we reconstructed the energy deposition spectrum generated by

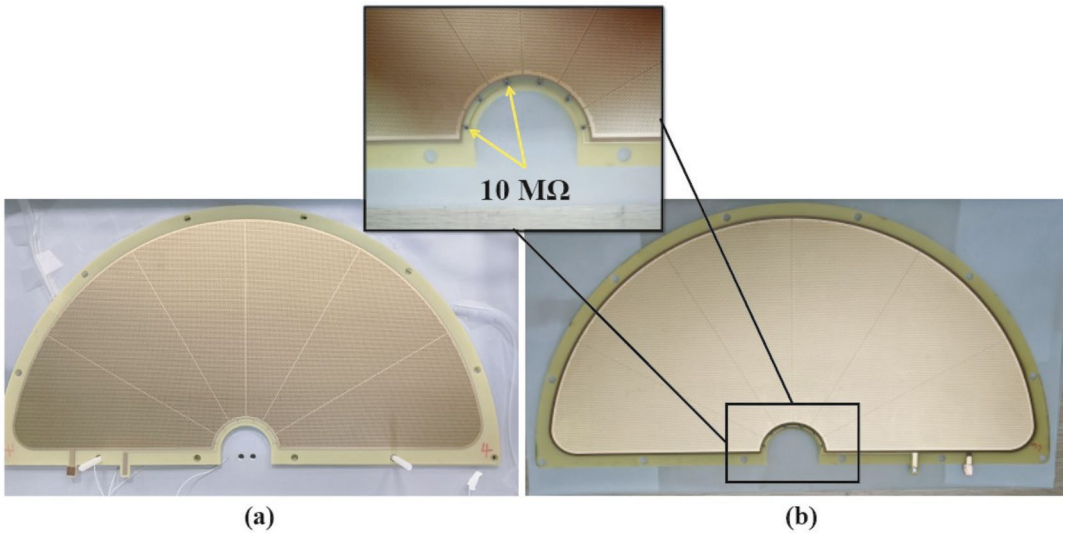

Fig. 4 (Color online) Unpartitioned side (**a**) and partitioned side (**b**) of THGEM

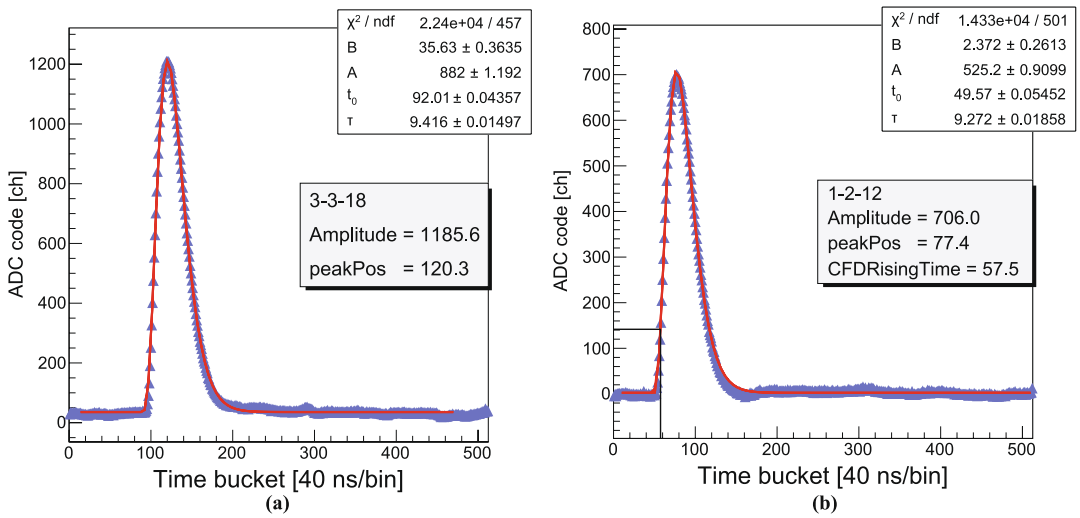

Fig. 5 Waveforms of the X-ray signal (**a**) and α particle signal (**b**), along with the fits of the electronics shaping function. The blue triangles represent the raw sampling points, and the red curves show the fitting function curves. The signal is digitized at a sampling rate of 25 MHz, with 512 12-bit samples, a peaking time of 1 µs and a trigger delay of 15 µs. The term "3-3-18" denotes the specific electronic channel: the 18th channel of the 3rd AGET chip on the 3rd front-end electronics board

the X-rays on each pad, as shown in Fig. 6. In the spectrum, the full-energy peak and the Ar escape peak of the X-ray are clearly visible. The escape peak is located at half the energy of the full-energy peak. Due to the small drift region, annihilation photons were more likely to escape from the sensitive region of the TPC, resulting in a higher count in the escape peak. The voltage of the cathode was set to 2400 V. With a THGEM operating voltage of −2500 V (−663 V for THGEM 1 and −612 V for THGEM 2), a sampling frequency of 25 MHz, and a shaping time of 1 µs, the scTPC achieved an energy resolution (FWHM) of approximately 22% for the 5.9 keV X-ray.

Due to factors such as the manufacturing process of the THGEM, detector assembly, readout electrode collection efficiency, transmission of the electronics, and data acquisition system, gain non-uniformity may occur across different channels. To characterize this non-uniformity, the full-energy peak position in the X-ray energy spectrum for each pad can be extracted. By normalizing the peak positions of all channels, the fluctuations between the channels can be calibrated, as shown in Fig. 7a. The gain fluctuations across

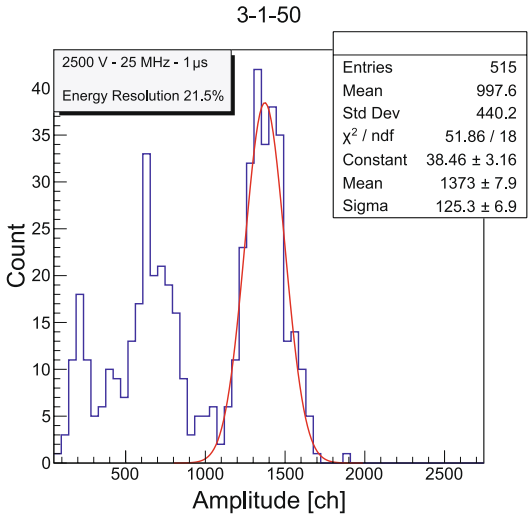

Fig. 6 Energy spectrum of the 5.9 keV X-ray on one pad

the readout plane reveal that the gain was relatively low for the central electrodes and high for the peripheral electrodes. This discrepancy may be due to differences in the tension experienced by the peripheral and central electrodes during the THGEM manufacturing process and detector assembly. When processing charged particle events, the normalized gain correction factors derived from the X-ray test, as shown in Fig. 7b, can be applied in the data analysis to partially correct for the degradation in energy measurement caused by channel fluctuations.

3.3 Drift velocity

The drift velocity of electrons in the scTPC drift region is crucial for the reconstruction of three-dimensional tracks of charged particles. Two methods were adopted to measure the drift velocity: The first method used a 266 nm UV laser. The laser beam was split into two beams through a half-lens (50% transmissive and 50% reflective). These two laser beams entered the drift region of the scTPC through two collimating holes (approximately 1 mm in diameter) on the inner wall of the field cage, and the drift velocity was calculated from the time difference between the two laser beams. Although attempts were made to keep both laser beams parallel to the readout plane, this was still difficult to achieve. There is still an angle between the two laser beams. Therefore, we extrapolated the two laser tracks back to their respective vertices (i.e., the positions of the two collimating holes). The distance between collimating holes was 16 cm. At each of the two collimating hole locations, there was a distinct and pronounced peak in the drift time, as shown in Fig. 8a. The drift velocity was calculated based on the time difference between collimating holes. The measured drift velocity was

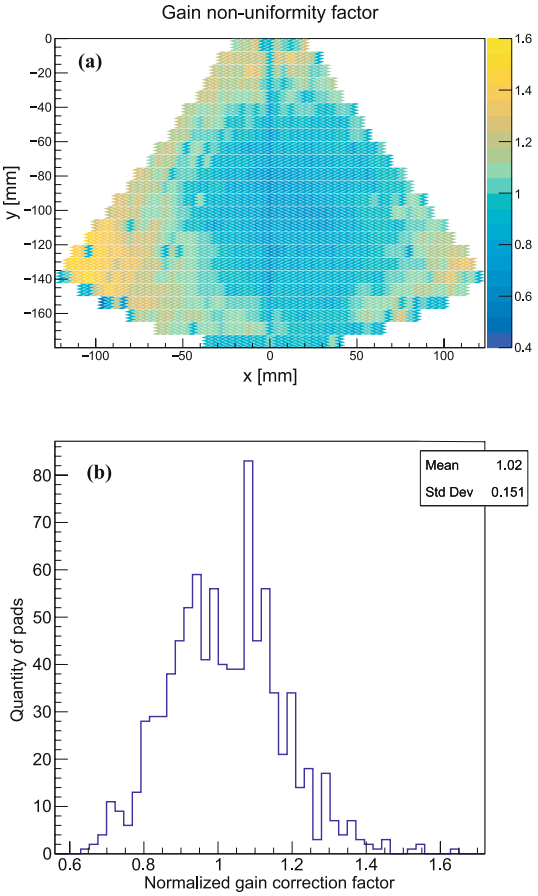

Fig. 7 (Color online) Maps of normalized gain (**a**) and gain correction factor (**b**) tested with the X-ray for the Ar (95%) + iC_4H_{10} (5%) gas mixture at local atmospheric pressure (850 mbar). The operating voltages for THGEM 1 and THGEM 2 were −650 V and −600 V, respectively

3.95 cm/μs under an electric field of 200 V/(cm atm) in an Ar(95%) + iC_4H_{10}(5%) gas mixture.

The second method utilizes cosmic ray muons to calculate drift velocity. There were no strict restrictions on the direction of the cosmic rays, which could pass through the scTPC from any position within the drift region. A 20 cm × 20 cm plastic scintillator was placed on the top side of the scTPC to serve as a trigger and provide a common zero time for all cosmic ray events. This setup allowed for the extraction of the time distribution in the drift direction for all cosmic ray tracks, as shown in Fig. 8b. The drift time exhibited a platform-like distribution, with steep leading and trailing edges indicating the closest point (infinitely close to the upper surface of THGEM 1) and the farthest point (infinitely close to the cathode surface) from the upper surface of THGEM 1, respectively. The leading and trailing edges were fitted using the following edge functions [43]:

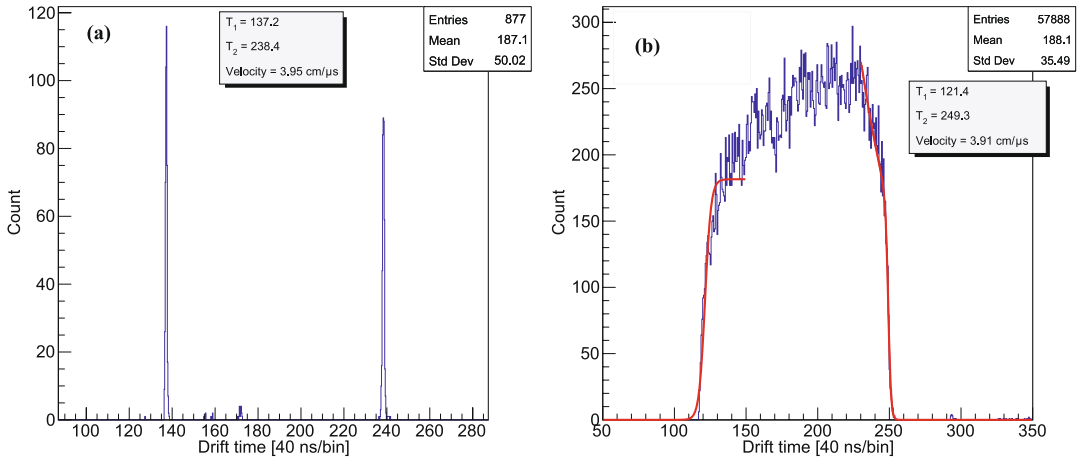

Fig. 8 Two methods of measuring the electron's drift velocity. Panel **a** shows the drift time distribution for two laser tracks at the vertex, with the left peak corresponding to the collimating hole with a drift length of 2 cm, and the right peak corresponding to another collimating hole with a drift length of 18 cm. Panel **b** depicts the drift time distribution for cosmic ray tracks, with the red curves representing the fitted curves for the rising and falling edges. The sampling frequency is 25 MHz. The operating gas is the Ar(95%) + iC_4H_{10}(5%) gas mixture at local atmospheric pressure (850 mbar). The reduced electric field in the drift region is 200 V/(cm atm)

$$f(t) = B + A\frac{e^{-t/\tau_1}}{1 + e^{(t-T_0)/\tau_2}}, \tag{3}$$

where T_0 is the time point of the leading edge (or the trailing edge), which corresponds to the point with the maximum slope. The time difference between the leading and trailing edges reflects the total length (20 cm) of the drift region. The measured drift velocity was 3.91 cm/μs under an electric field of 200 V/(cm atm) in an Ar(95%) + iC_4H_{10}(5%) gas mixture. The drift velocities obtained by both methods are in close agreement, and the drift velocity calculated using Garfield++ [44] is 4.12 cm/μs. The deviation between the calculated and measured results may be attributed to the presence of gas impurities.

The equipment for measuring drift velocity using a laser is complex and only provides the drift velocity at a specific position. In contrast, the method using cosmic rays offers a simpler setup for characterizing the average drift velocity. Since a flow-type gaseous chamber is used, the gas pressure in the chamber fluctuates with the external air pressure, and the purity of the operating gas may vary. Consequently, calibration of the electron drift velocity is essential for each test and experiment. Using cosmic rays, real-time measurement of the drift velocity can be performed easily and quickly.

3.4 Track reconstruction

The particle track is three-dimensional and can be projected onto the *xy*-plane and *zy*-plane. The *x*-axis is aligned with the pad row, and the *y*-axis is aligned with the pad column, as shown in Figs. 2c and 7a. The *z*-axis represents the direction of the drift electric field, opposite to the drift direction of the electron and perpendicular to the readout plane. The *xy*-plane is parallel to the readout plane, while the *zy*-plane is perpendicular to it. A pad with a detected signal is classified as a hit, with the *x*- and *y*-coordinates of the hit corresponding to the geometric center of the pad in the horizontal and vertical directions, respectively. All hits in the same row are grouped into a cluster. The *y*-coordinates of the cluster are defined as the *y*-coordinates of the row, while the *x*-coordinates are the average of the *x*-coordinates of all hits, weighted by the deposited charge (i.e., Amplitude). The *z*-coordinates of the hits are calculated by multiplying the drift time by the drift velocity, which is 3.91 cm/μs as determined in Sect. 3.3. The drift time is calculated from the leading edge of the signal waveform relative to the zeroth time bucket, i.e., CFDRisingTime as shown in Fig. 5b. Since the drift time is not an absolute value, it must be referenced to a common zero point. The *z*-coordinate of the cluster is the average of the *z*-coordinates of all hits, weighted by the Amplitude. The reconstructed track is a straight line that fits through a series of clusters.

The track resolution consists of the spatial resolution on the *xy*-plane (referred to as *x*-resolution) and the spatial resolution on the *zy*-plane (referred to as *z*-resolution). The spatial resolution was evaluated using the residuals, which represent the distance from the charge center of the cluster to the fitted track line. For example, in the *xy*-plane,

$$\text{residual}_x = \frac{ky_i + b - x_i}{\sqrt{(k^2+1)}}, \tag{4}$$

where (x_i, y_i) represents the charge center of the cluster, and k and b are the parameters of the fitted track line. The

standard deviation σ (referred to as the standard deviation throughout the text) of the residual distribution is defined as the x-resolution [23, 45]. The same approach is applied to the zy-plane. Track reconstruction and position resolution measurements of long tracks for the scTPC were performed using cosmic ray muons and heavy-ion beams.

3.5 Cosmic ray test

Cosmic ray muons traverse the scTPC in stochastic directions and positions, enabling a comprehensive assessment of the overall performance of the scTPC. The energy deposition from cosmic rays within the scTPC is low, leading to a suboptimal signal-to-noise ratio. As a result, higher amplification is necessary to clearly detect the cosmic ray track. This amplification may cause unrelated hits to accompany the muon track, resulting in positional inaccuracies (Fig. 9a). Additionally, due to the large size of the plastic scintillators, there are instances when multiple tracks are detected within the same sampling time window, though such occurrences are rare. Therefore, track recognition must be performed prior to track reconstruction [46–51]. To address this challenge, we employ the Hough transform for track recognition and derive a flag value ddd in the Hough space to distinguish between effective and ineffective hits [52, 53]. A hit with a d value within a specific range is considered effective, and the judgment condition is determined by analyzing the ddd-distribution of multiple tracks. The Hough transform has been widely applied and extended to particle track recognition due to its simple and intuitive transformation method. The particle under investigation in our future experiments exhibits characteristics similar to cosmic rays, specifically long tracks that penetrate the TPC, with typically only one track present per event. In such cases, the classical Hough transform is effective for recognizing and reconstructing secondary particle tracks. The original coordinate system (x, y, z) (in Euclidean space) is consistent with the coordinate system defined in Sect. 3.4 and Fig. 2c.

The (x, y) coordinates of hits in Euclidean space are first transformed into Hough space, where a point in Euclidean space corresponds to a curve in the Hough space. When multiple hits lie along the same linear track, their corresponding curves in Hough space intersect at a common point. In contrast, the Hough curves of ineffective hits located away from the track do not converge at this common point, as shown in Fig. 9a and b. The coordinates of the common point in Hough space, ($\theta_{xy,\mathrm{com}}$, $r_{xy,\mathrm{com}}$), were determined, and the minimum distance d_{xy} from each

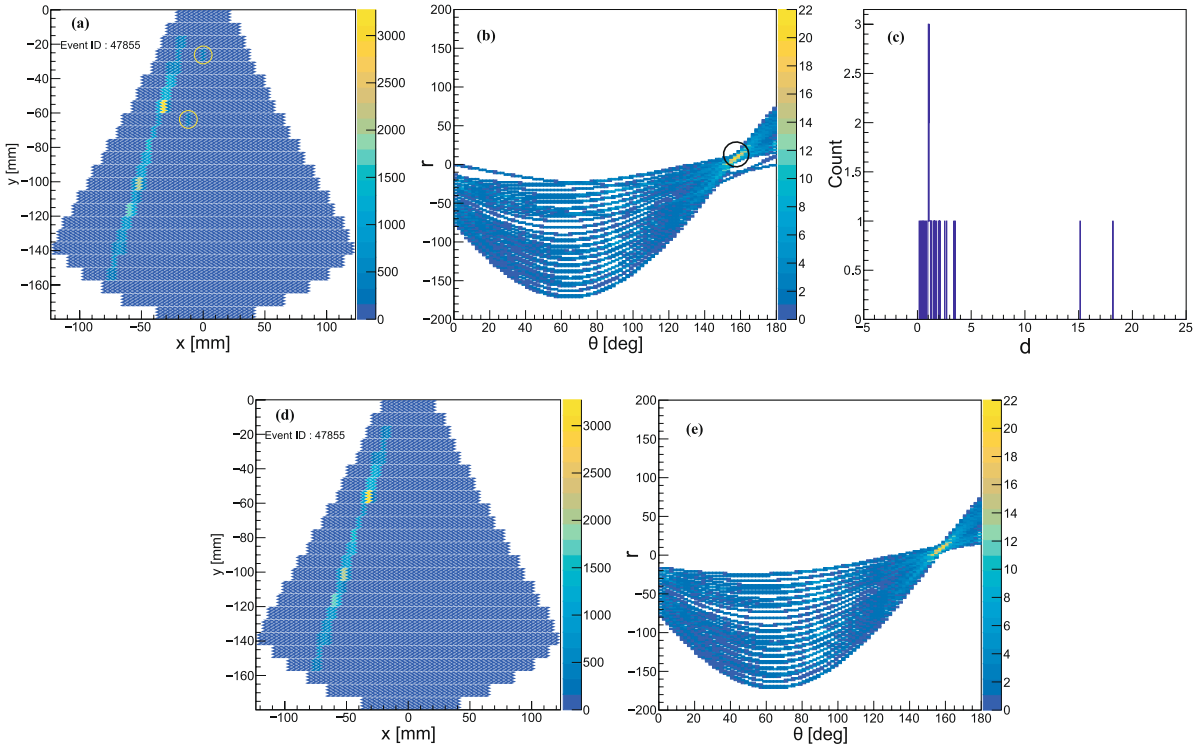

Fig. 9 (Color online) Hough transform and track recognition on the xy-plane are shown in the following figures. The hit distribution in Euclidean space is presented in panel (**a**), where the stray hit is highlighted in the yellow circle. Panel **b** shows the hit distribution in Hough space, with the common point indicated by a black circle. Panel **c** depicts the d_{xy} distribution of one track. The hit distribution after track recognition in Euclidean space is shown in panel (**d**), and panel **e** displays the corresponding hit distribution after recognition in Hough space

Hough curve to the common point was calculated. For a point on the track, its d_{xy} value should be nearly equal to or slightly greater than zero, while the d_{xy} value of a stray point will be larger, as illustrated in Fig. 9c. After comparing across multiple tracks, points with $d_{xy} \leq 4.0$ are considered effective hits, while those with $d_{xy} > 4.0$ are deemed ineffective. After applying this d_{xy} discrimination, stray hits can be rejected, and track recognition can be successfully achieved on the xy-plane, as shown in Fig. 9d and e. Note that this threshold may require adjustment depending on the detector design and the complexity of events involving multiple tracks.

Track recognition on the zy-plane using the Hough transform follows a similar approach. The (z, y) coordinates of the hits in Euclidean space are transformed into Hough space, as shown in Fig. 10. The coordinates of the common point in Hough space, ($\theta_{zy,\mathrm{com}}$, $r_{zy,\mathrm{com}}$), are determined, and the minimum distance d_{zy} from each Hough curve to the common point is calculated. On the zy-plane, points with $d_{zy} \leq 2.0$ are considered effective hits, while points with $d_{zy} > 2.0$ are deemed ineffective.

With the discrimination by d_{xy} and d_{zy} based on the Hough transform, stray hits are discarded. The residual distributions on the xy-plane and zy-plane were then extracted to observe the x and z-resolutions of the cosmic ray track, as shown in Fig. 11. The residual distribution did not follow a standard Gaussian function. Therefore, we fit the residual distribution with the sum of two Gaussian functions, both with means close to zero. The fitting function [54] is expressed as:

$$f(x) = \frac{A_1}{\sqrt{2\pi}\sigma_1}\exp\left(-\frac{(x-\mu_1)^2}{2\sigma_1^2}\right) + \frac{A_2}{\sqrt{2\pi}\sigma_2}\exp\left(-\frac{(x-\mu_2)^2}{2\sigma_2^2}\right), \tag{5}$$

where A_1 and A_2 are the integrals of the two Gaussian functions, μ_1 and μ_2 are their means, and σ_1 and σ_2 are the standard deviations of the two Gaussian functions. The track resolution is determined as the weighted root mean square (RMS) of σ_1 and σ_2, given by:

$$\sigma_x = \sqrt{\frac{A_1\sigma_1^2 + A_2\sigma_2^2}{A_1 + A_2}}. \tag{6}$$

If the residual distribution can be accurately fitted by a single Gaussian function, the track resolution is considered to

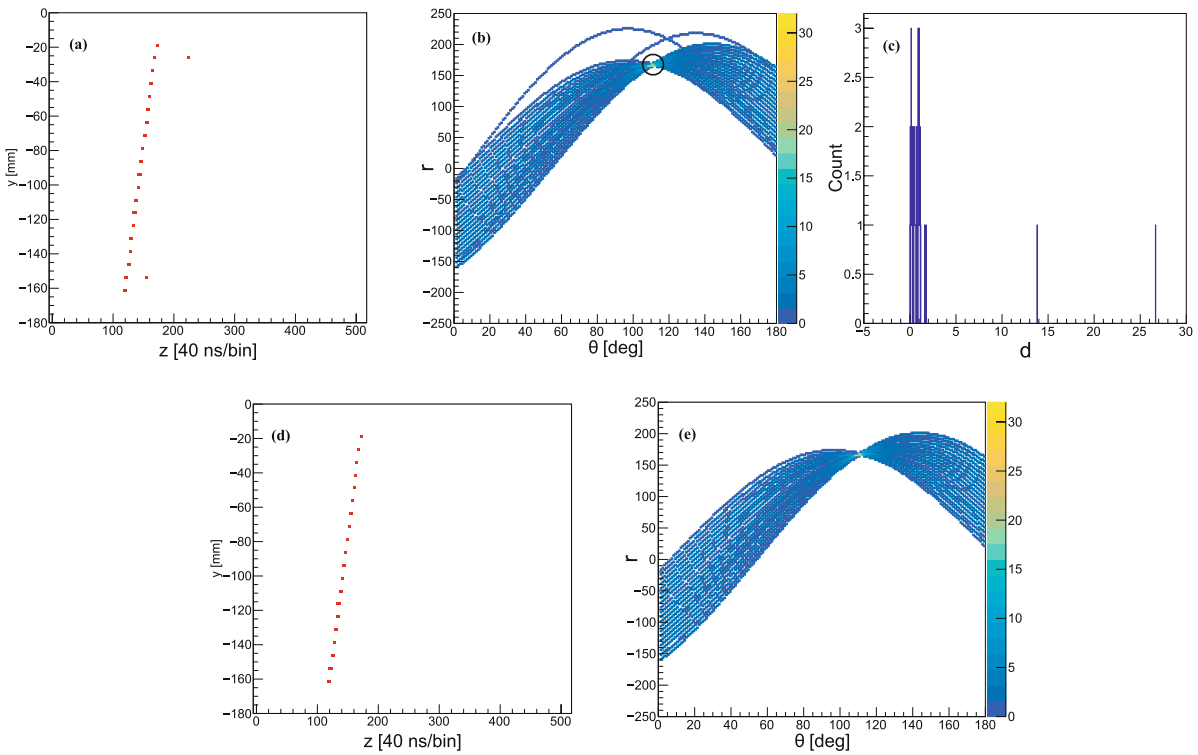

Fig. 10 (Color online) Hough transform and track recognition on the zy-plane are illustrated in the following figures. Panel **a** shows the hit distribution in Euclidean space, while panel **b** presents the hit distribution in Hough space, with the common point circled by a black circle. Panel **c** depicts the d_{zy} distribution of one track. The hit distribution after track recognition in Euclidean space is shown in panel (**d**), and panel **e** displays the hit distribution after recognition in Hough space

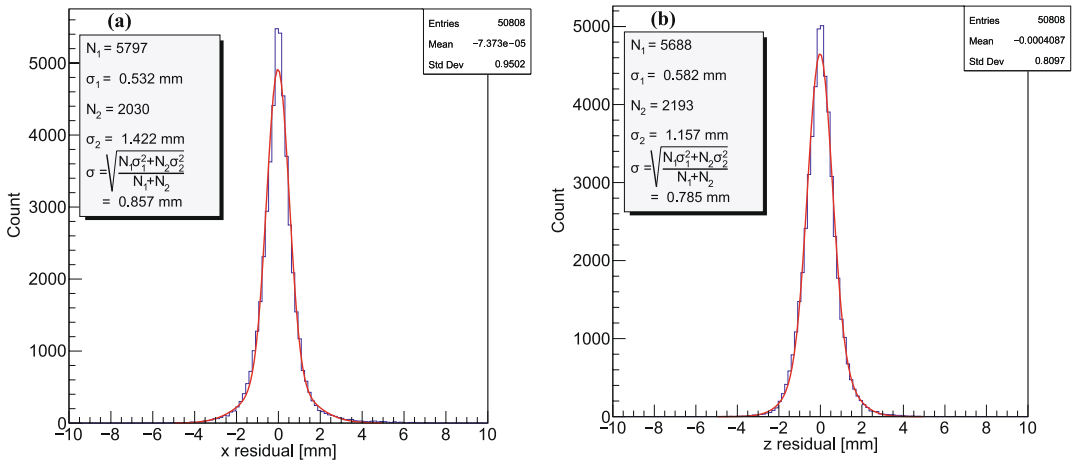

Fig. 11 Residual distributions of the muon track on the *xy*-plane (**a**) and *zy*-plane (**b**). For the cosmic ray track, the *x*-resolution is 0.86 mm, and the *z*-resolution is 0.79 mm. The red curves represent the double-Gaussian fitting functions

be simply given by the standard deviation σ of that Gaussian. However, if the distribution exhibits more complexity and cannot be described by a single Gaussian, two Gaussian functions are employed to fit the residual distribution, as explained previously. For the cosmic ray tracks, efficient tracks were identified and reconstructed. This resulted in a track resolution of 0.86 mm in the *x*-direction and 0.79 mm in the *z*-direction. Additionally, in the *z*-direction, an angular resolution of approximately 0.2° for θ was achieved, considering a typical track length of about 20 cm. This level of precision is critical for several applications, such as calibrating the energy-θ relationship of triton generated from (^{3}He,*t*) nuclear reactions and reconstructing the angular distribution of the cross section.

3.6 Beam test

To validate the functionality of the scTPC in the presence of a heavy-ion beam background, a beam test was conducted at the HIRFL. The detector was fully assembled, as shown in Fig. 12. A non-polarized ^{3}He gas target, encapsulated in a sealed stainless-steel container with three atmospheres of ^{3}He gas (providing an effective target thickness of approximately 2.2×10^{21} atoms/cm^2), was positioned at the center of the scTPC. The cylindrical stainless-steel container measured 20 cm in length and 3.8 cm in diameter, with a sidewall thickness of 200 µm (i.e., the exit window for secondary particles was 200 µm thick). The two end faces of the container, each 2 mm thick, served as the incoming and outgoing windows for the beam. Given that the beam energy is high but the intensity is low, the energy loss in the beam windows is minimal compared to the total energy of the beam, rendering the heating power negligible. The target was placed on a 3D-printed holder to ensure that its center axis was aligned with the center of the beam. The heavy-ion beam did not pass through the TPC but instead passed through the ^{3}He target. Large-angle scattering of secondary particles penetrated the sidewall of the stainless-steel container and entered the scTPC. The detector was housed in a stainless-steel chamber. The beam used was a 350 MeV/u Kr beam with an intensity of approximately 10^6 particles per second. The beam entered the chamber through a 25 µm thick window made of aluminized Mylar film with a 40 mm diameter. It then passed through a second 25 µm thick window of aluminized Mylar film, this time with a 55 mm diameter, before exiting the chamber. Eight CsI(Tl) crystals, each with a thickness of 2 cm and a length of 20 cm, were positioned in a curved array around the scTPC outside. The signals from the CsI(Tl) crystals were sequentially extracted, amplified, and discriminated using a preamplifier (Mesytec MPR-16) and a shaping/timing filter amplifier (Mesytec MSCF-16). After an OR operation, the signals from the eight crystals

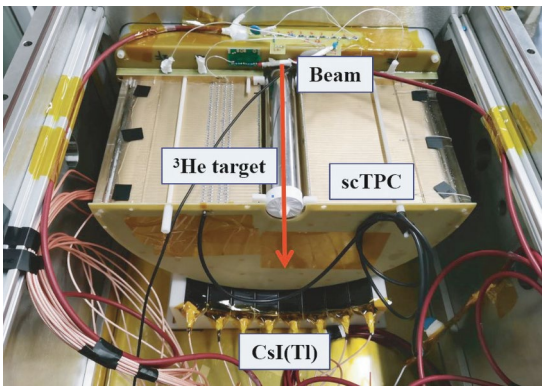

Fig. 12 (Color online) Complete setup for the detector assembly of the beam test. The red line is the direction of the beam

were converted into TTL signals to trigger the AGET. Consequently, the scTPC signal recorded by the AGET corresponds to the long track traversing the scTPC and the energy deposited in the CsI(Tl) crystals.

As shown in Fig. 13, the track is often accompanied by a number of background particles, primarily distributed in the upper part of the readout electrode (near the target). Therefore, track recognition is crucial for the data analysis of beam tests. Track recognition based on the Hough transform is used to reconstruct the particle track, as shown in Fig. 14, with $d_{xy} \leq 4.0$ and $d_{zy} \leq 2.0$, consistent with the cosmic ray track. The residual distribution of secondary particle tracks was fitted using a double-Gaussian function, as shown in Fig. 15, resulting in x- and z-resolutions of 0.71 mm and 0.73 mm, respectively, for the beam test. These results are consistent with the cosmic ray test outcomes. The angular resolution of the scattering angle, θ, can reach 0.2°. Good angular resolution is essential for establishing a precise relationship between the scattering angle and the differential cross section in the center-of-mass system, particularly for specific points in the cross section, such as local maxima or minima. The detailed shape of the angular distribution aids in better extrapolation of measurements to small-angle scattering regions and reduces extrapolation errors. Due to limitations such as the duration of the beam test, the triton could not be identified. However, the test successfully verified the operation of the detector. First, the scTPC operated normally without discharging under the high background environment caused by the heavy-ion beam and maintained sufficient performance. Second, the CsI(Tl) signal was used to trigger the AGET and effectively detect secondary particle tracks.

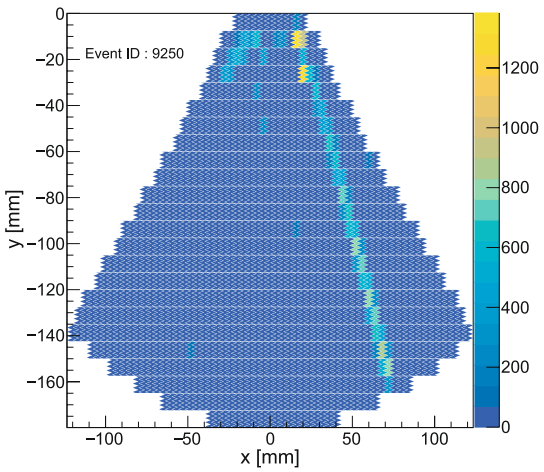

Fig. 13 (Color online) Distribution of raw hits on the xy-plane of a long track produced by the secondary particle under the heavy-ion beam test

A Kr-beam experiment was performed to validate the performance of the detector. We were interested in C and O isotopes instead of Kr. Although small-angle scattering near 0° in the center-of-mass frame provides more detailed information on the transition dynamics and nuclear structure, detecting tritons is technically challenging because the kinetic energy of a triton approaches zero in the laboratory frame at this angle range. Consequently, nuclear reaction experiments were designed to measure the recoiled triton with a relatively large kinetic energy in inverse kinematics. Then, combined with the angular distribution of the reaction cross section calculated theoretically, the data for the small-angle range were extrapolated from the measured result to the greatest extent possible. According to the Geant4 simulation [21], the current detector system can measure triton with $E_{\mathrm{t,lab}} > 20$ MeV and $\theta_{\mathrm{t,lab}} < 85°$, considering the energy loss of triton in the insensitive zone of the detector (including the

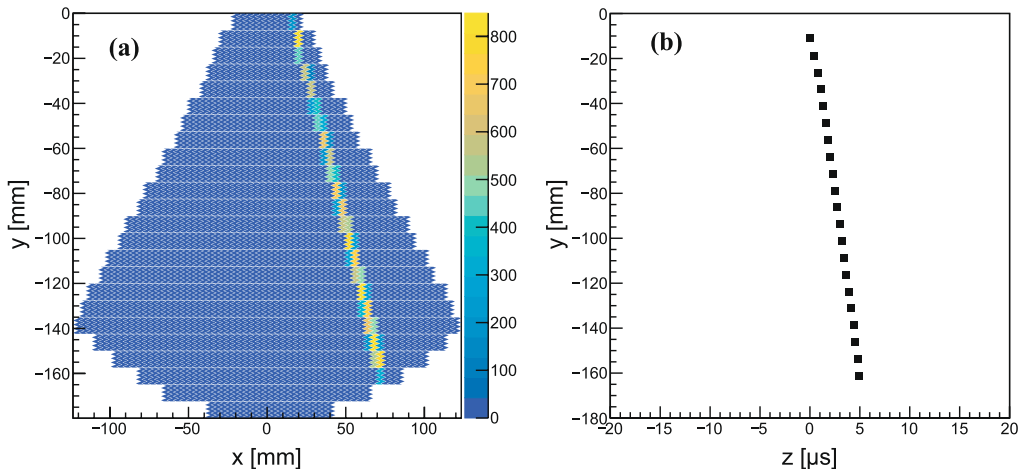

Fig. 14 (Color online) Projections on the xy-plane (**a**) and zy-plane (**b**) after the track recognition of a long track produced by the secondary particle under the heavy-ion beam test

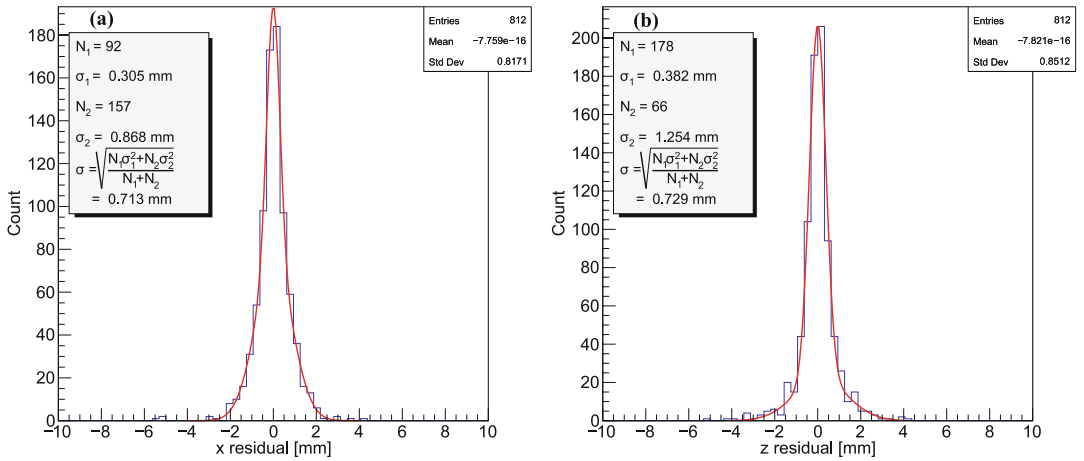

Fig. 15 Residual distributions of secondary particle tracks under the heavy-ion beam test are shown for the *xy*-plane (**a**) and *zy*-plane (**b**). The *x*-resolution is 0.71 mm, and the *z*-resolution is 0.73 mm. The red curves represent the double-Gaussian fitting functions

target window and the field cage structure). The maximum energy deposition of triton in CsI(Tl) was approximately 140 MeV, as determined by the thickness of CsI(Tl).

The background from δ electrons must be considered for control and veto in beam experiments. The maximum kinetic energy that can be transferred in a single collision is limited and depends on the kinetic energy of the incident particle. For an incident nucleus with a kinetic energy of 500 MeV/u, the calculated maximum kinetic energy of the δ electron is approximately 1.4 MeV. The results from Geant4 simulations (Fig. 16) and kinematic calculations are in good agreement. As the kinetic energy of the δ electron increases, its generation probability decreases. The vast majority of δ electrons will not enter the TPC, as they are blocked by the ^{3}He target sidewall and the scTPC field cage structure. Those δ electrons that do enter the sensitive region of the detector can be rejected by the CsI(Tl) because they cannot trigger the CsI(Tl). In addition, δ electrons either do not enter the scintillators, or the energy they deposit in the scintillators is generally below the trigger threshold.

According to theoretical calculations (see the preprint [55]), for a ^{20}O beam with an intensity of 10^6 particles per second, the yield rate of our charge-exchange reaction (transition between isobaric analog states) is approximately 10 particles per hour in three atmospheres of ^{3}He gas. To achieve the statistical precision required for the experiment (over 1000 counts), approximately 100 h of beam time were needed to accumulate the data.

4 Summary

This study focuses on the performance of the scTPC. The energy resolution and gain non-uniformity of the THGEM were tested using a ^{55}Fe X-ray source. The drift velocity of

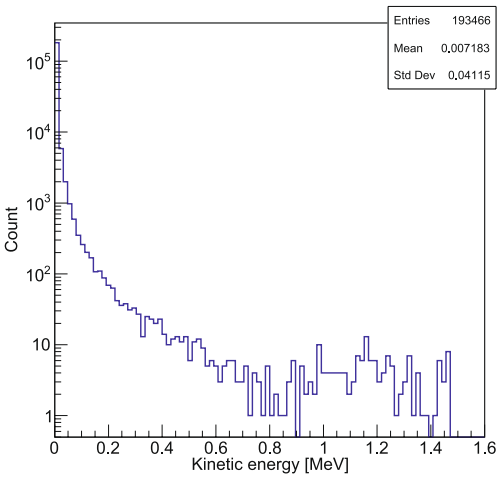

Fig. 16 Energy spectrum of the δ electron simulated by Geant4

the electrons was measured using both a laser and cosmic ray muons. At a reduced electric field of 200 V/(cm atm), the drift velocity was 3.95 cm/μs from the laser test and 3.91 cm/μs from the cosmic ray test. The position resolution of the long track was measured using cosmic rays and heavy-ion beams. For the cosmic ray tracks, the position resolution was 0.86 mm on the *xy*-plane and 0.79 mm on the *zy*-plane, resulting in an angular resolution better than 0.2°. In the heavy-ion beam test, the beam bombarded the ^{3}He target, and secondary charged particles were measured with the scTPC. For the secondary particles, the position resolution was 0.71 mm on the *xy*-plane and 0.73 mm on the *zy*-plane, yielding an angular resolution better than 0.2°. The performance of the scTPC meets the requirements for measuring the product particles of the (^{3}He,*t*) reaction and supports the next stage of the experiment.

Author contributions All authors contributed to the study conception and design. Material preparation, data collection and, analysis were performed by Zhi-Xuan He, Pan-Jiao Shen, Jing-Yan Wang, and Wen-Juan Bu. The first draft of the manuscript was written by Zhi-Xuan He, and all authors commented on previous versions of the manuscript. All authors read and approved the final manuscript.

Data availability The data that support the findings of this study are openly available in Science Data Bank at https://cstr.cn/31253.11.sciencedb.j00186.00513 and https://www.doi.org/10.57760/sciencedb.j00186.00513.

Declarations

Conflict of interest The authors declare that they have no conflict of interest.

References

1. H. Fujimura, H. Akimune, I. Daito et al., Nuclear structure of the spin-isospin excited states in ^{13}N studied via the (^{3}He,t) and (^{3}He,tp) reactions at 450 MeV. Phys. Rev. C **69**, 064327 (2004). https://doi.org/10.1103/PhysRevC.69.064327
2. J. Li, Y.J. Li, Z.H. Li et al., Nuclear astrophysics research based on HI-13 tandem accelerator. Nucl. Tech. (in Chinese) **46**(8), 080002–1 (2023). https://doi.org/10.11889/j.0253-3219.2023.hjs.46.080002
3. H.J. Wörtche, A.M. van den Berg, V.M. Hannen et al., High resolution studies of low lying GT strength using the (d,^{2}He) reaction and its impact on electron-capture rates in stellar environments. Nucl. Phys. A **719**, C131–C134 (2003). https://doi.org/10.1016/S0375-9474(03)00982-5
4. R.G.T. Zegers, T. Adachi, H. Akimune et al., Extraction of weak transition strengths via the (^{3}He,t) reaction at 420 MeV. Phys. Rev. Lett. **99**(20), 202501 (2007). https://doi.org/10.1103/PhysRevLett.99.202501
5. K. Yako, H. Sakai, S. Yoshida et al., Charge exchange spin-dipole excitations of ^{90}Zr and the neutron skin thickness. Nucl. Phys. A **788**, 273 (2007). https://doi.org/10.1016/j.nuclphysa.2007.01.013
6. D. Frekers, P. Puppe, J.H. Thies et al., Gamow-Teller strength extraction from (^{3}He,t) reactions. Nucl. Phys. A **916**, 219 (2013). https://doi.org/10.1016/j.nuclphysa.2013.08.006
7. B.M. Loc, N. Auerbach, D.T. Khoa, Single-charge exchange reactions and the neutron density at the surface of the nucleus. Phys. Rev. C **96**, 014311 (2017). https://doi.org/10.1103/PhysRevC.96.014311
8. J.J. Li, D.Y. Pang, Y.L. Ye et al., Improved Eikonal approach for charge exchange reactions at intermediate energies. Chin. Phys. C **43**, 124202 (2019). https://doi.org/10.1088/1674-1137/43/12/124102
9. J.J. Li, C.A. Bertulani, Y. Liu et al., Eikonal method for charge-exchange reactions at intermediate energies. Phys. Rev. C **102**, 064601 (2020). https://doi.org/10.1103/PhysRevC.102.064601
10. B. Gao, R.G.T. Zegers, J.C. Zamora et al., Gamow-Teller transitions to ^{93}Zr via the ^{93}Nb(t,^{3}He+γ) reaction at 115 MeV/u and its application to the stellar electron-capture rates. Phys. Rev. C **101**, 014308 (2020). https://doi.org/10.1103/PhysRevC.101.014308
11. B. Gao, S. Giraud, K.A. Li et al., New ^{59}Fe stellar decay rate with implications for the ^{60}Fe radioactivity in massive stars. Phys. Rev. Lett. **126**, 152701 (2021). https://doi.org/10.1103/PhysRevLett.126.152701
12. S. Giraud, J.C. Zamora, R.G.T. Zegers et al., Simulations and analysis tools for charge exchange (d,^{2}He) reactions in inverse kinematics with the AT-TPC. Nucl. Instrum. Methods Phys. A **1051**, 168213 (2023). https://doi.org/10.1016/j.nima.2023.168213
13. S. Giraud, J.C. Zamora, R.G.T. Zegers et al., β^+ Gamow-Teller strengths from unstable ^{14}O via the (d,^{2}He) reaction in inverse kinematics. Phys. Rev. Lett. **103**, 232301 (2023). https://doi.org/10.1103/PhysRevLett.130.232301
14. J.Y. Xu, Z.Z. Li, B.H. Sun et al., Constraining equation of state of nuclear matter by charge-changing cross section measurements of mirror nuclei. Phys. Lett. B **833**, 137333 (2022). https://doi.org/10.1016/j.physletb.2022.137333
15. G.S. Li, J. Su, B.H. Sun et al., New measurement of the elemental fragmentation cross sections of 218 MeV/u 28Si on a carbon target. Phys. Rev. C **107**, 024609 (2023). https://doi.org/10.1103/PhysRevC.107.024609
16. Y.Z. Sun, S.T. Wang, Z.Y. Sun et al., Two-neutron removal cross sections from ^{15,16}C at around 240 MeV/u. Phys. Rev. C **99**, 024605 (2019). https://doi.org/10.1103/PhysRevC.99.024605
17. Y.X. Zhao, Y.Z. Sun, S.T. Wang et al., One-proton knockout from ^{16}C at around 240 MeV/u. Phys. Rev. C **100**, 044609 (2019). https://doi.org/10.1103/PhysRevC.100.044609
18. Y.Z. Sun, S.T. Wang, Z.Y. Sun et al., Single-neutron removal from ^{14,15,16}C near 240 MeV/u. Phys. Rev. C **104**, 014310 (2021). https://doi.org/10.1103/PhysRevC.104.014310
19. W.H. Ma, J.S. Wang, Y.Y. Yang et al., Experimental study of the ^{9}Li breakup reaction on Pb target. Nucl. Sci. Tech. **28**, 177 (2017). https://doi.org/10.1007/s41365-017-0334-4
20. Y.J. Yuan, D.Q. Gao, L.Z. Ma et al., Present status of HIRFL complex in Lanzhou. J. Phys. Conf. Ser. **1401**, 012003 (2020). https://doi.org/10.1088/1742-6596/1401/1/012003
21. Z.X. He, M. Li, W.J. Bu et al., Development of a semi-cylindrical time projection chamber prototype for (^{3}He,t) charge exchange reaction experiment. Eur. Phys. J. C **83**, 1092 (2023). https://doi.org/10.1140/epjc/s10052-023-12170-x
22. G. Li, J.L. Lou, Y.L. Ye et al., Property investigation of the wedge-shaped CsI(Tl) crystals for a charged-particle telescope. Nucl. Instrum. Methods Phys. A **1013**, 165637 (2021). https://doi.org/10.1016/j.nima.2021.165637
23. F. Sauli, *Gaseous Radiation Detectors: Fundamentals and Applications* (Cambridge University Press, Cambridge, 2023). https://doi.org/10.1017/CBO9781107337701
24. R. He, X.Y. Niu, Y. Wang et al., Advances in nuclear detection and readout techniques. Nucl. Sci. Tech. **34**, 205 (2023). https://doi.org/10.1007/s41365-023-01359-0
25. H.K. Wu, X.Y. Wang, Y.M. Wang et al., Fudan multi-purpose active target time projection chamber (fMeta-TPC) for photonuclear reaction experiments. Nucl. Sci. Tech. **35**, 200 (2024). https://doi.org/10.1007/s41365-024-01576-1
26. X.G. Cao, Y.L. Chang, K. Chen et al., NνDEx-100 conceptual design report. Nucl. Sci. Tech. **35**, 3 (2024). https://doi.org/10.1007/s41365-023-01360-7
27. J.Y. Xu, Q.T. Li, Y.L. Ye et al., Performance of a small AT-TPC prototype. Nucl. Sci. Tech. **29**, 97 (2018). https://doi.org/10.1007/s41365-018-0437-6
28. L.S. Yang, J.Y. Xu, Q.T. Li et al., Performance of the CAT-TPC based on two-dimensional readout strips. Nucl. Sci. Tech. **32**, 85 (2021). https://doi.org/10.1007/s41365-021-00919-6
29. W. Huang, F. Lu, H. Li et al., Laser test of the prototype of CEE time projection chamber. Nucl. Sci. Tech. **29**, 41 (2018). https://doi.org/10.1007/s41365-018-0382-4
30. J. Tian, Z.P. Sun, S.B. Chang et al., Studies of an event-building algorithm of the readout system for the twin TPCs in

HFRS. Nucl. Sci. Tech. **35**, 73 (2024). https://doi.org/10.1007/s41365-024-01434-0
31. Y. Li, Y. Han, Y.K. Sun et al., Performance study of the multi-purpose time projection chamber (MTPC) using a four-component alpha source. Nucl. Instrum. Methods Phys. Res. A **1060**, 169045 (2024). https://doi.org/10.1016/j.nima.2023.169045
32. T.R. Gentile, P.J. Nacher, B. Saam et al., Optically polarized ^{3}He. Rev. Mod. Phys. **89**, 045004 (2017). https://doi.org/10.1103/RevModPhys.89.045004
33. B.T. Kim, T. Udagawa, Intermediate energy charge-exchange reactions induced by polarized ^{3}He. Nucl. Instrum. Methods Phys. A **402**, 354–360 (1998). https://doi.org/10.1016/s0168-9002(97)00862-0
34. Y. Zhang, X. Qian, B.T. Hu, Density measurement through elastic electron scattering with a gaseous target at the Jefferson Lab. Chin. Phys. C **36**, 610 (2012). https://doi.org/10.1088/1674-1137/36/7/008
35. A. Breskin, R. Alon, M. Cortesi et al., A concise review on THGEM detectors. Nucl. Instrum. Methods Phys. A **598**, 107 (2009). https://doi.org/10.1016/j.nima.2008.08.062
36. A. Breskin, M. Cortesiet, R. Alon, The THGEM: a thick robust gaseous electron multiplier for radiation detectors. Nucl. Instrum. Methods Phys. A **623**, 132 (2010). https://doi.org/10.1016/j.nima.2010.02.172
37. S. Bachmann, A. Bressan, M. Capeáns et al., Discharge studies and prevention in the gas electron multiplier (GEM). Nucl. Instrum. Methods Phys. Res. A **479**, 294–308 (2002). https://doi.org/10.1016/S0168-9002(01)00931-7
38. B. Azmoun, P. Garg, T.K. Hemmick et al., Design studies for a TPC readout plane using zigzag patterns with multistage GEM detectors. IEEE Trans. Nucl. Sci. **65**(7), 1416 (2018). https://doi.org/10.1109/TNS.2018.2846403
39. E.C. Pollacco, G.F. Grinyer, F. Abu-Nimeh et al., GET: a generic electronics system for TPCs and nuclear physics instrumentation. Nucl. Instrum. Methods Phys. Res. A **887**, 81–93 (2018). https://doi.org/10.1016/j.nima.2018.01.020
40. C. Li, C.Q. Feng, D.Y. Zhu et al., An optical fiber-based flexible readout system for micropattern gas detectors. J. Instrum. **13**, P04013 (2018). https://doi.org/10.1088/1748-0221/13/04/P04013
41. G. Song, M. Shao, L.L. Shang et al., Production and properties of a charging-up "Free" THGEM with DLC coating. Nucl. Instrum. Methods Phys. Res. A **966**, 163868 (2020). https://doi.org/10.1016/j.nima.2020.163868
42. Z.Y. Li, X.Y. Ai, Y.G. Xie et al., Study on gain stability of thick gas electron multiplier. Nucl. Instrum. Methods Phys. Res. A **986**, 164534 (2021). https://doi.org/10.1016/j.nima.2020.164534
43. H. Yi, Z. Zhang, Z.G. Xiao et al., Prototype studies on the forward MWDC tracking array of the external target experiment at HIRFL-CSR. Chinese Phys. C **38**, 126002 (2014). https://doi.org/10.1088/1674-1137/38/12/126002
44. Garfield++, https://garfieldpp.web.cern.ch/garfieldpp/
45. R.K. Carnegie, M.S. Dixit, J. Dubeau et al., Resolution studies of cosmic-ray tracks in a TPC with GEM readout. Nucl. Instrum. Methods Phys. A **538**, 372–383 (2005). https://doi.org/10.1016/j.nima.2004.08.132
46. M.Y. Liu, W.D. Wu, X.T. Huang et al., Simulation and reconstruction of particle trajectories in the CEPC drift chamber. Nucl. Sci. Tech. **35**, 128 (2024). https://doi.org/10.1007/s41365-024-01497-z
47. Z.L. Liao, X.G. Cao, Y.X. Yang et al., Design and construction of charged-particle telescope array for study of exotic nuclear clustering structure. Nucl. Sci. Tech. **35**, 134 (2024). https://doi.org/10.1007/s41365-024-01503-4
48. W. Jiang, P. Cao, Y.M. Wu et al., FPGA-based position reconstruction method for neutron beam flux spatial distribution measurement in BNCT. Nucl. Sci. Tech. **35**, 56 (2024). https://doi.org/10.1007/s41365-024-01417-1
49. D.W. Si, Y. Zhou, S. Xiao et al., Measurement of the high energy γ -rays from heavy ion reactions using Cerenkov detector. Nucl. Sci. Tech. **35**, 24 (2024). https://doi.org/10.1007/s41365-024-01368-7
50. Y. Liu, X.C. Ai, G.Y. Xiao et al., Simulation study of BESIII with stitched CMOS pixel detector using acts. Nucl. Sci. Tech. **34**, 203 (2023). https://doi.org/10.1007/s41365-023-01353-6
51. Y.L. Chen, H.K. Wang, S.Y. Zhang et al., Hi'CT: a pixel sensor-based device for ion tomography. Nucl. Sci. Tech. **34**, 111 (2023). https://doi.org/10.1007/s41365-023-01251-x
52. R.O. Duda, P.E. Hart, Use of the hough transformation to detect lines and curves in pictures. Commun. ACM **15**(1), 11–15 (1972). https://doi.org/10.1145/361237.361242
53. R. Frühwirth, A. Strandlie, *Pattern Recognition, Tracking and Vertex Reconstruction in Particle Detectors* (Springer International Publishing, Berlin, 2021). https://doi.org/10.1007/978-3-030-65771-0
54. C.M.S. Collaboration, Performance of the CMS cathode strip chambers with cosmic rays. J. Instrum. **5**, T03018 (2010). https://doi.org/10.1088/1748-0221/5/03/T03018
55. Z.X. He, W.J. Bu, C.Y. Chao et al., Study of (^{3}He,t) charge exchange reactions to isobaric analog states in inverse kinematics. arXiv. https://doi.org/10.48550/arXiv.2307.10643